Shear strain imaging using shear deformations

Min Rao,[a)] Tomy Varghese, and Ernest L. Madsen
*Department of Medical Physics, The University of Wisconsin—Madison, 1300 University Avenue,
1530 MSC, Madison, Wisconsin 53706*

In this article we investigate the generation of shear strain elastograms induced using a lateral shear deformation. Ultrasound simulation and experimental results demonstrate that the shear strain elastograms obtained under shear deformation exhibit significant differences between bound and unbound inclusions in phantoms, when compared to shear strain images induced upon an axial compression. A theoretical model that estimates the decorrelation between pre- and postdeformation radio frequency signals, as a function of extent of shear deformation, is also developed. Signal-to-noise ratios of shear strain elastograms obtained at different shear angles are investigated theoretically and verified using ultrasound simulations on a uniformly elastic phantom. For the simulation and experiment, a two-dimensinal block-matching-based algorithm is used to estimate the axial and lateral displacement. Shear strains are obtained from the displacement vectors using a least-squares strain estimator. Our results indicate that the signal-to-noise ratio (SNR) of shear strain images increases to reach a maximum and saturates, and then decreases with increasing shear angle. Using typical system parameters, the maximum achievable SNR for shear strain elastography is around 8 (18 dB), which is comparable to conventional axial strain elastography induced by axial compression. Shear strain elastograms obtained experimentally using single inclusion tissue-mimicking phantoms with both bound and unbound inclusions (mimicking cancerous masses and benign fibroadenomas, respectively) demonstrate the characteristic differences in the depiction of these inclusions on the shear strain elastograms. © *2008 American Association of Physicists in Medicine*. [DOI: 10.1118/1.2825621]

I. INTRODUCTION

Pathological changes in tissue generally correlate with changes in tissue elastic modulus.[1] Elastography, as a strain imaging technique, has gained interest as a diagnostic tool over the past decade.[2–8] In this technique, local strains are typically estimated along the axial direction corresponding to the ultrasonic beam propagation axis by computing the gradient of the tissue displacement following a uniaxial compression. The mappings of such axial strains, referred to as axial-strain elastograms, are usually utilized as a surrogate for the tissue modulus distribution. Elastography has been shown to be capable of tumor detection in breast[9] and prostate.[10] However, some benign lesions, such as fibroadenomas in the breast, have similar modulus distributions as infiltrating ductal carcinomas.[11] Hence, axial strain imaging alone may not provide sufficient information to assess the malignancy of a detected lesion.

Some progress has been made in using elastography to distinguish benign from malignant tumors. Garra *et al.*[9] have shown that discrepancies between the size of lesions on sonograms and axial strain images may be a promising way to distinguish benign from malignant lesions. Malignant lesions tend to be depicted as larger masses on axial strain images than on sonograms, while benign lesions usually appear smaller or of the same size on sonograms as on the axial strain images. As described in Garra *et al.*,[9] this discrepancy

in size between benign fibroadenomas and malignant cancerous lesions is probably due to axial strain images also depicting regions around the tumor that have undergone desmoplastic reaction as stiffer regions reflecting the underlying change[9] that is not captured on the sonograms. Another significant difference between fibroadenomas and cancers involves a difference in binding to the surrounding tissues.[9,12] Previous studies[13,14] have shown that malignant breast tumors typically have a stellate or spiculated appearance and are firmly bound to the surrounding tissue through infiltration, whereas fibroadenomas (the most common benign breast tumor) have smoother margins and are more loosely bound to the surrounding tissue and in some instances may be surrounded by a capsule.

Konofagou *et al.*,[12] using axial compressions, have shown that the shear strain estimates may provide supplementary information on the bonding between the tumor and the surrounding tissue characterizing different tissue elements based on their mobility. However, the amount of shear strain obtained under an axial compression, as presented in previous work,[12] is usually very small (on the order of 0.01 for a 1%−3% compression) and difficult to control. In addition, shear strain elastograms of bound and unbound inclusions may exhibit similar patterns due to the axial compression applied. Figure 1 shows an example of shear strain images calculated using finite element analysis (FEA) of a fully
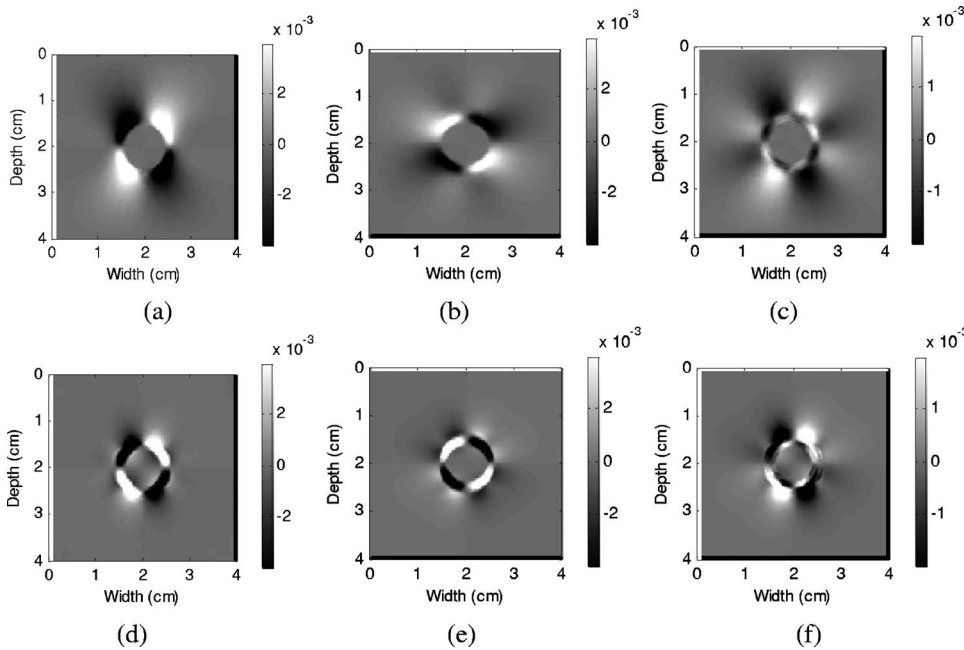
FIG. 1. Finite-element calculated images of [(a) and (d)] $\partial d_z / \partial x$, [(b) and (e)] $\partial d_x / \partial z$, and [(c) and (f)] shear strain$=0.5(\partial d_z / \partial x + \partial d_x / \partial z)$, where d_z and d_x are the displacements in the z (axial) and x (lateral) directions, respectively, for a fully bound inclusion (top) and an unbound inclusion (bottom) in a homogeneous background. The applied axial strain was 1%.

bound inclusion (top) and an unbound inclusion (bottom) in a homogeneous background. The bound inclusion is used to simulate a malignant tumor, with the spherical inclusion and the background glued together in the FEA model. The unbound inclusion model is utilized to simulate an encapsulated benign lesion with no adhesion between the spherical inclusion and the surrounding background medium. Both the spherical inclusions are three times stiffer than the background and the applied axial strain is 1%. Observe that the shear strain patterns of the bound and unbound inclusions have some differences, which, however, may be obscured in the presence of noise artifacts, making it difficult to differentiate between benign and malignant tumors *in vivo*.

In this study, we investigate shear strain elastograms (SSEs) induced by a lateral shear deformation instead of an axial compression. Although there are prior studies[15,16] on shear strain elastography induced by shear deformation, no simulation or experimental results have been presented to assess its ability for differentiating bound from unbound inclusions. Kumar *et al.*[16] analyzed signal decorrelation induced by shear deformation by assuming that the displacement remained constant within the ultrasonic beam. However, this assumption is valid only when the applied deformation is small and the beam is relatively narrow. In this article, a closed form expression is derived for the correlation coefficient between pre- and postdeformation ultrasonic radio frequency (rf) signals. Signal decorrelation due to shear deformation effects within the ultrasonic beam has also been considered in this article. Noise performance of shear strain estimates are discussed theoretically and verified using ultrasound (US) simulations on a uniformly elastic phantom. US simulation and tissue-mimicking (TM) phantom experiments were also performed to demonstrate the feasibility and

advantage of using shear strain images induced by a lateral shear deformation to distinguish benign from malignant tumors.

II. NOISE PERFORMANCE ANALYSIS

In conventional elastography, signal decorrelation noise, due to the distortion of the echo signal as a result of the applied axial compression, is a major source of error in the local strain estimated.[17–25] Similarly, SSEs induced by a shear deformation also suffer from decorrelation between pre- and postdeformation rf signals. The amount of shear deformation is quantified by the lateral shear angle θ, as shown in Fig. 2. For large shear angles, the shear decorrelation noise artifacts are significant. For the small shear angle, however, the induced shear strain may be too small to provide useful information. Thus, it is important to choose an optimal shear angle in order to achieve a SSE with a high image quality. Many studies have been performed to investigate variations in spatial correlations with ultrasound
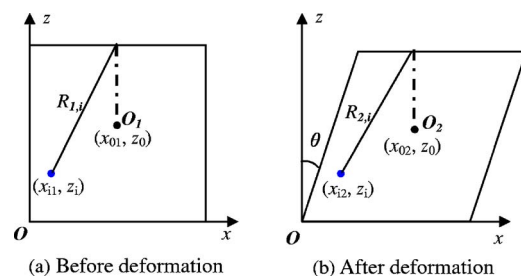

FIG. 2. Schematic diagram illustrating the acquisition of pre- and postdeformation rf signals with a shear angle θ. The predeformation rf signals are obtained from scatterers at position O_1, while the postdeformation signals are obtained from the corresponding scatterers at location O_2.

speckle pattern motion in medical ultrasonic images.[26–33] Most of these prior studies were directed toward *B*-mode image compounding or blood flow imaging, where the theories developed did not incorporate signal decorrelation within finite gated windows, and were thus not suitable for computing the correlation coefficient for shear strain imaging induced by shear deformations.

To evaluate the performance of shear strain imaging, several groups have proposed the estimation of the correlation coefficient between the rf signals acquired before and after the application of the shear deformation.[15,16] Viola and Walker[15] derived the correlation coefficient with motion compensation due to shear deformation. However, no explicit expression was provided and the theory was not verified using simulations or experiments. Kumar *et al.*[16] developed an expression for the correlation coefficient that depends on both the axial compression and shear deformation. Their expression was obtained by making an approximation based on their previous work[22] derived for axial compression analysis. In addition, optimal shear deformation has not been discussed in the above articles. To investigate the shear angle dependence on the SSE image quality, we derive a theoretical model to estimate the correlation coefficient between pre- and postdeformation rf signal segments as a function of the shear angle. We also derive the signal-to-noise ratio (SNR) for SSE. The theoretical results are verified using US simulations on a uniformly elastic phantom.

II.A. Correlation coefficient

Ultrasonic rf echo signals before and after the shear deformations are modeled by

$$s_1(x,z) = P(x,z) \otimes T_1(x,z),$$

$$s_2(x,z) = P(x,z) \otimes T_2(x,z), \tag{1}$$

where the subscripts 1 and 2 specify the pre- and postdeformation echo signals obtained from an elastic tissue medium, $P(x,z)$ is the pulse-echo point-spread function (PSF) of the imaging system, and $T(x,z)$ denotes the tissue scattering function. For this model it is assumed that the system is linear and has a shift invariant impulse response which holds within a small volume of interest (5×5 mm^2) at the focus.[34] The symbol $\otimes$ denotes the convolution operation. Here a two-dimensional (2D) model is used because the ultrasound beam in currently available transducers is much wider in the elevational direction when compared to the lateral direction. In addition, the elevational displacement is very small and can be neglected for lateral shear deformation. Thus, the scatterer movement in the elevational direction does not cause significant loss of coherence in the echoes.

There are several models that define the $T(x,z)$ term. To simplify the tissue model, we assume a large number of very small inhomogeneities (Rayleigh scatterers) with respect to the wavelength of the PSF (Ref. 20)

$$T_1(x,z) = \sum_i |T_i| \delta(x - x_i, z - z_i),$$

$$T_2(x,z) = \sum_i |T_i| \delta(x - x_i - z_i \tan \theta, z - z_i), \tag{2}$$

where $\delta(x,z)$ is the 2D Dirac or impulse function, (x_i, z_i) denotes the randomly distributed centers of each inhomogeneity, $|T_i|$ is the echogenicity of each scatterer, and θ is the angle of shear deformation, as defined in Fig. 2.

The cumulative signal amplitude from scatterers at position O_1 (x_{01}, z_0) in the predeformation medium can be written as[26]

$$s_1 = \sum_i |T_i||P_{1,i}| \exp(j\vartheta_i). \tag{3}$$

The subscript i refers to an individual scatterer, $|P|$ is the magnitude of the pulse-echo PSF from the scatterers, and $\exp(j\vartheta)$ represents the combined phase of $|T|$ and $|P|$. The phase factors in ϑ are uniformly distributed over 2π rad with zero mean. Here we assume narrowband signals for simplifying the mathematical analysis. An illustration of this concept is shown in Fig. 2. We establish our coordinates by setting the bottom-left corner of the phantom as the origin.

A shear deformation is then applied to the medium along the x direction, with the scatterers moving laterally with a shear angle θ. To maintain volume of the medium, axial displacements would also be induced by the lateral shear deformation. FEA simulations, which are described in Sec. IV, show that the axial displacement induced is quite small and only occurs at the lateral edges of the medium. Assuming that the region of interest is located at the center of the medium, axial displacements at the region of interest would be close to zero and can therefore be ignored in our analysis. Thus, tissue scatterers around O_1 move to position O_2 after the shear deformation, as shown in Fig. 2. The postdeformation signal is generated from scatterers at position O_2 (x_{02}, z_0). The cumulative signal strength after the shear deformation can be written as

$$s_2 = \sum_i |T_i||P_{2,i}| \exp(j\vartheta_i)\exp(j\Delta\phi_i), \tag{4}$$

where $\Delta\phi_i$ is the phase difference between pre- and postdeformation signals, which can be written as $4\pi(R_{2,i} - R_{1,i})/\lambda_0$, where λ_0 is the wavelength at the center frequency and $R_{1,i}$, $R_{2,i}$ are the distances from the ith scatterer to the transducer for the pre- and postdeformation situations, respectively,

$$R_{1,i} = \sqrt{(x_{i1} - x_{01})^2 + (z_i - h)^2},$$

$$R_{2,i} = \sqrt{(x_{i2} - x_{02})^2 + (z_i - h)^2}, \tag{5}$$

where $x_{02} = x_{01} + z_0 \tan \theta$, $x_{i2} = x_{i1} + z_i \tan \theta$, and h is the height of the phantom. The cross correlation between the signals acquired before and after deformation can be written as[26]

$$\langle s_1 s_2^* \rangle = \sum_i |T_i|^2 |P_{1,i}||P_{2,i}| \exp(j\Delta\phi_i). \tag{6}$$

The 2D PSF in the focal zone of each ultrasound beam of a linear array transducer can be expressed in the following form:

$$|P(x,z)| = p_x(x)p_z(z), \tag{7}$$

where p_x represents the lateral beam spread function and p_z represents the axial spread function. For a rectangular aperture, for example, the lateral PSF for a pulse-echo response at the focus or in the far field can be written as

$$p_x(x) = \sin^2(\pi f_0 x)/(\pi f_0 x)^2, \tag{8}$$

where $f_0 = D/r\lambda_0$, D is the effective transducer aperture, and r is the focal distance, $r = h - z_0$. If we assume that the ultrasound pulse transmitted by the transducer has a Gaussian envelope with characteristic width σ_z, then p_z can be expressed as

$$p_z(z) = \exp(-z^2/2\sigma_z^2). \tag{9}$$

For the ith scatterer, the lateral distances to the beam axis for the pre- and postdeformation cases can be written as

$$l'_{1,i} = x_i - x_{01},$$

$$l'_{2,i} = x_{i2} - x_{02}. \tag{10}$$

Similarly, the axial distances from the ith scatterer to the center point are

$$l''_{1,i} = l''_{2,i} = z_i - z_0. \tag{11}$$

Hence, the PSF for the ith scatterer can be written as

$$P_{k,i} = p_x(l'_{k,i})p_z(l''_{k,i}), \quad (k = 1,2). \tag{12}$$

Substituting Eq. (12) into Eq. (6), and going to a continuous representation, x_i and z_i become x and z and the summation becomes a 2D integral about x and z. Thus,

$$\langle s_1 s_2^* \rangle = B' \iint |p_x(l'_1)||p_z(l''_1)||p_x(l'_2)||p_z(l''_2)| \exp(j\Delta\phi)dxdz, \tag{13}$$

where B' is a normalization factor. An analytical closed form solution for the above equation is difficult to obtain. Thus, it is necessary to either resort to numerical solutions or apply approximations to simplify the expression in Eq. (13).

To simplify the 2D integral in Eq. (13), we utilize a Gaussian envelope with characteristic width σ_x, to model the lateral PSF as shown

$$p_x(x) = \exp(-x^2/2\sigma_x^2). \tag{14}$$

Since only scatterers close to the region of interest contribute to the signal, we can approximate the phase term as $\exp[2\pi j(l_2'^2 - l_1'^2)/\lambda_0(h - z_0)]$. The correlation coefficient can be computed as follows:

$$\rho_0 = \frac{\langle s_1 s_2^* \rangle}{\sqrt{\langle s_1 s_1^* \rangle \langle s_2 s_2^* \rangle}}. \tag{15}$$

Substituting Eqs. (9) and (14) into Eq. (13), and then plugging the result into Eq. (15), we obtain

$$\rho_0 = \left[\frac{4\pi^2 \sigma_x^2 \sigma_z^2 \tan^2\theta}{\lambda_0^2(z_0 - h)^2} + \frac{\sigma_z^2 \tan^2\theta}{4\sigma_x^2} + 1 \right]^{-1/2}. \tag{16}$$

Equation (16) provides an expression for the correlation coefficient between the pre- and postdeformation signals acquired from the point of interest O_1 and O_2, respectively. For elastographic processing, finite gated segments of the echo signal are utilized. A gated data segment is generally selected using a rectangular window. Generally, the same window is used for both the pre- and postdeformation data segments. Attenuation and focusing effects can be included in the window function $w(t)$, so that the intensity of $s(t)$ can be taken to be constant with depth. Thus, the correlation coefficient between the pre- and postdeformation data segments can be computed by[35]

$$\rho_{1,2} = \frac{\langle \sum_{t=t1}^{t2} w^2(t)s_1(t)s_2^*(t) \rangle}{[\langle \sum_{t=t1}^{t2} w^2(t)s_1(t)s_1^*(t) \rangle \langle \sum_{t=t1}^{t2} w^2(t)s_2(t)s_2^*(t) \rangle]^{1/2}}. \tag{17}$$

The overall signal intensity obtained before and after the shear deformation should be the same, provided that the distance between the transducer and sample volume remains constant. The denominator in Eq. (17) becomes[35]

$$\left[\left\langle \sum_{t=t1}^{t2} w^2(t)s(t)s^*(t) \right\rangle \left\langle \sum_{t=t1}^{t2} w^2(t)s(t)s^*(t) \right\rangle \right]^{1/2}$$

$$= \left\langle \sum_{t=t1}^{t2} w^2(t)s(t)s^*(t) \right\rangle. \tag{18}$$

The ensemble average operator can be moved inside the summation. As mentioned above, attenuation and focusing effects are included in the $w(t)$ term so that the intensity of $s(t)$ is constant with depth. Equation (18) becomes

$$\sum_{t=t1}^{t2} \langle w^2(t)s(t)s^*(t) \rangle = \bar{I} \cdot \sum_{t=t1}^{t2} w^2(t), \tag{19}$$

where $\bar{I} = \langle s \cdot s^* \rangle$ is the mean signal intensity. Replacing the summation with an integral, Eq. (17) becomes

$$\rho_{1,2} = \frac{\int_{t_1}^{t_2} w^2(t)\langle s_1(t)s_2^*(t) \rangle/\bar{I}dt}{\int_{t_1}^{t_2} w^2(t)dt}$$

$$= \frac{\int_{-Z/2}^{Z/2} w^2(\xi)\langle s_1(\xi)s_2^*(\xi) \rangle/\bar{I}d\xi}{\int_{-Z/2}^{Z/2} w^2(\xi)d\xi}$$

$$= \frac{\int_{-Z/2}^{Z/2} w^2(\xi)\rho(\xi)d\xi}{\int_{-Z/2}^{Z/2} w^2(\xi)d\xi}, \tag{20}$$

where Z is the window length of the windowed rf echo signal segment, ξ is the distance from a position within the window to the center of the window, which is in the range from $-Z/2$ to $Z/2$. $\rho(\xi)$ is the correlation of signals resulting from position ξ within the window of the rf segment. Since the axial coordinate of position ξ is $z_0 + \xi$, the axial distance from the ith scatterer to position ξ becomes $l''_{1,i} = l''_{2,i} = z_i - (z_0 + \xi)$. Substituting these new axial distances into Eq. (13) and performing the integration, we can obtain the correlation coefficient between signal samples located at position ξ within the window of the rf segment as

$$\rho(\xi) = \rho_0 \exp\left[-\frac{\xi^2}{\sigma_z^2}(1-\rho_0^2)\right]. \tag{21}$$

So far we have only considered the ideal condition where the lateral displacement is accurately tracked and the point of interest is always at the center of a beam line. Under practical conditions, however, the beam lines are not continuous but sampled. The center point O_2 in Fig. 2 may not exactly be in the center of a beam after a shear deformation. To take this effect into account, we assume the presence of a shift Δl between the beam axis and the position of O_2 in the lateral direction. So the lateral distances from scatterers to the beam axis for the postdeformation case can be written as

$$l'_{2,i} = x_{i2} - x_{02} - \Delta l. \tag{22}$$

Substituting Eq. (22) into Eq. (13) and performing the integration, we can obtain the modified correlation coefficient for signals resulting from position ξ within the window of the rf segment as

$$\rho'(\xi) = \rho_0 \exp\left[-\frac{(\xi - \Delta l/\tan\theta)^2}{\sigma_z^2}(1-\rho_0^2)\right]. \tag{23}$$

II.B. Signal-to-noise ratio

The SNR of shear strain elastograms can be defined in a similar way as the SNR_e of axial elastograms and is given by

$$\text{SNR}_{\text{sse}} = \frac{\varepsilon_{\text{sse}}}{\sigma_{\text{sse}}}, \tag{24}$$

where ε_{sse} and σ_{sse} are, respectively, the mean and standard deviation of the shear strains over a region of uniform elasticity. The shear strain is defined by

$$e_{zx} = \frac{1}{2}\left(\frac{\partial d_z}{\partial x} + \frac{\partial d_x}{\partial z}\right), \tag{25}$$

where d_z and d_x denote, respectively, the axial and lateral displacement. From this definition, the variance of the shear strain can be expressed in terms of the variance of axial and lateral displacement, $\sigma^2(d_z)$ and $\sigma^2(d_x)$,

$$\sigma_{\text{sse}}^2 = \frac{\sigma^2(d_z)}{X\Delta x} + \frac{\sigma^2(d_x)}{Z\Delta z}, \tag{26}$$

where X denotes the lateral beam width, Δx is the beam spacing, and Δz is the window separation in the axial direction. Although the lateral displacement would be related to the axial displacement by the Poisson's ratio for incompressible materials, the estimation of the axial and lateral displacements from the ultrasound echo signals have been assumed to be independent of each other to simplify the derivation. The upper bound of the SNR_{sse} is obtained when the lower bound on the displacement estimation standard deviation[36] is substituted in Eq. (26),

$$\sigma^2(d_z)_{\text{ZZLB}} \geq \begin{cases} \dfrac{(sT)^2}{12}, & (BT)\text{SNR}_C < \gamma \\[2mm] \text{threshold} & \gamma < (BT)\text{SNR}_C < \delta \\[2mm] \sigma^2(d_z)_{\text{BB}} = \dfrac{18f_c^2}{\pi^2 T(B^5 + 12B^3 f_c^2)}\left[\dfrac{1}{\rho^2}\left(1+\dfrac{1}{\text{SNR}^2}\right)^2 - 1\right], & \delta < (BT)\text{SNR}_C < \mu \\[2mm] \text{threshold} & \mu < (BT)\text{SNR}_C < \eta \\[2mm] \sigma^2(d_z)_{\text{CRLB}} = \dfrac{3}{2\pi^2 T(B^3 + 12Bf_c^2)}\left[\dfrac{1}{\rho^2}\left(1+\dfrac{1}{\text{SNR}^2}\right)^2 - 1\right], & \eta < (BT)\text{SNR}_C \end{cases}, \tag{27}$$

where γ, δ, μ, and η are thresholds,[36] that demarcate the three distinct operating regions of the Ziv–Zakai lower bound (ZZLB) for the time delay or displacement estimation variance based on the value of the postintegration SNR term $BT\,\text{SNR}_C$, s denotes the strain, T is the axial window length in units of time, B is the bandwidth, f_c is the center frequency, ρ is the correlation coefficient, which is given by Eq. (20), and the SNR term represents only the contribution due to electronic noise (SNR_S). A distinct threshold region (where an exponential increase in the variance occurs) is observed between the Cramer–Rao lower bound (CRLB) and the Barankin bound (BB) and the constant variance level. Accurate estimation of the displacement and strain is possible only within the CRLB. The composite SNR_C incorpo-

rates both the electronic noise and the decrease in SNR caused by signal decorrelation and is given by[36]

$$\text{SNR}_C = \frac{\text{SNR}_S \text{SNR}_\rho}{1 + \text{SNR}_S + \text{SNR}_\rho}, \tag{28}$$

where $\text{SNR}_\rho = \rho/(1-\rho)$.

The variance of the lateral displacement estimates can be expressed in terms of the variance of the axial displacement estimates[37]

$$\sigma^2(d_x) \approx \left(\frac{X}{l_p}\right)^2(1+3/b_l^2)\sigma^2(d_z), \tag{29}$$

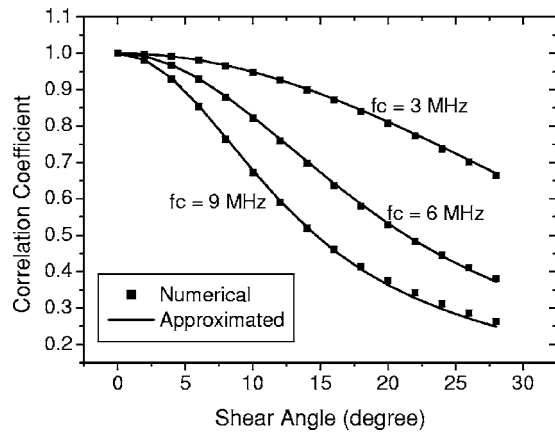where l_p is the pulse width and b_l is the fractional bandwidth.

FIG. 3. Comparison between the exact numerical and approximated theoretical expressions for the correlation coefficient vs shear angle for different insonification frequencies.
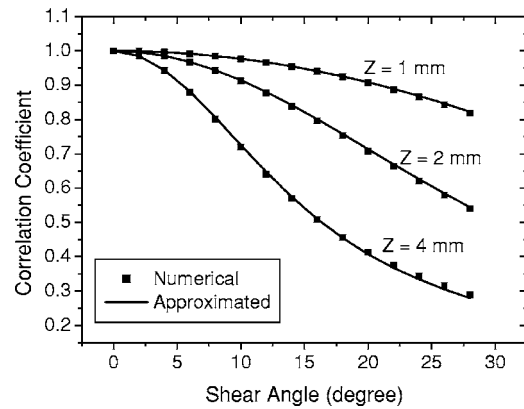

FIG. 4. Comparison between the exact numerical and approximated theoretical expressions for the correlation coefficient vs shear angle for different rf data segment lengths.

Thus, the lower bound on the variance of the shear strain can be obtained by substituting Eqs. (27) and (29) into Eq. (26). Observe from Eqs. (27)–(29) that the variance of axial and lateral displacement estimates strongly depends on the effective correlation coefficient ρ. In this article, we derive the effective correlation coefficient of pre- and postdeformation rf segments as a function of the amount of lateral shear deformation applied. The effects of finite window length on signal decorrelation and on variance of the strain estimator are taken in consideration, which is more accurate and complete than the method used in the prior study.[16]

The correlation model presented in this article can be easily extended to study the signal decorrelation caused by other types of deformation, such as axial compression, lateral expansion, and axial shear deformation, etc. Axial compression, which is usually applied in conventional elastography, is not addressed in this study. This is because the shear strain images obtained by applying an axial compression exhibit similar patterns for both bound and unbound inclusions, as shown in Fig. 1. In addition, the image quality of SSEs will be decreased due to the additional decorrelation noise caused by the axial compression if both axial compression and lateral shear deformation are applied simultaneously.

III. THEORETICAL RESULTS

Figure 3 presents a comparison of the correlation coefficient obtained from the numerical integration of Eq. (13) and the approximate expression obtained using Eqs. (16), (20), and (21). Here we ignored signal intensity variations due to attenuation and focusing effects and the window function $w(t) \equiv 1$. The correlation coefficients are plotted as a function of the shear angle for different insonification frequencies. Results were obtained using a 3-mm rf segment centered at a depth of 2 cm and the transducer aperture was 10 mm. To approximate the lateral PSF using a Gaussian profile, we used $\sigma_x = 0.36/f_0$ in Eq. (14) to match the main lobe of the beam profile given in Eq. (8). As shown in the figure, a good agreement between the approximated curves (solid lines) and the numerical results (square symbols) is demonstrated. This

indicates that the Gaussian profile provides a good approximation of the lateral PSF and the effect of beam sidelobes on signal decorrelation can be ignored. As illustrated in the figure, the signal decorrelation rate of rf signal pairs increases with the insonification frequency. This is primarily due to the fact that the ultrasound beam becomes narrower with increased frequency, enabling scatterers that were within the predeformation beam to leave the beam and newer scatterers to enter the beam after the lateral shear deformation, especially at large shear angles.

Figure 4 presents the normalized correlation coefficient values for different lengths of rf signal segments. Both the numerical and approximated results are plotted and they agree with each other. The rf data segment was assumed to be centered at a 2-cm depth in the phantom, the aperture of the transducer was assumed to be 10 mm, and the insonification frequency 6 MHz. As the length of the rf segment increases, the scatterers included within the gated segment are farther from the center of the initial data segment. Now, with the application of the shear deformation, new scattering sources are interrogated, especially for depths around the edges of the gated region, causing the signal to decorrelate faster.

IV. METHODS AND RESULTS

It is more convenient to study the noise performance of the shear strain estimates using a uniformly elastic phantom. However, shear strain elastograms for inclusion phantoms are needed to investigate the ability of shear strain imaging in assessing tumor malignancy. In this work, computer simulations and phantom experiments were used to demonstrate the feasibility of using shear strain images induced by a lateral shear deformation to distinguish benign from malignant tumors.

IV.A. Simulation

A uniformly elastic simulated TM phantom to evaluate the noise performance of shear strain imaging along with two simulated single-inclusion phantoms of dimensions 4

$\times 4$ cm^2 were constructed using FEA software (ANSYS, Inc., Canonsburg, USA), with a Poisson's ratio of 0.495 assumed for both the inclusion and the background for all phantoms.

Both inclusion phantoms contain a 1-cm diameter inclusion, which was three times stiffer than the background. The model is two dimensional, so that the inclusions correspond to cylinders perpendicular to the scan plane. The first inclusion phantom simulated the case of a malignant tumor, with the inclusion fully bound to the surrounding medium. The second inclusion phantom simulated the case of a benign tumor, with the inclusion loosely bound to the background. This was implemented in ANSYS by creating a contact surface between the inclusion and background with a friction coefficient of 0.01. The density of the mesh utilized for the ANSYS simulated phantom was varied in the phantom, with regions closer to the boundary of the inclusion meshed with comparatively higher density (to obtain more accurate FEA predictions of the local displacement), since we are more interested in the shear strains generated at the interface between the background and the inclusion. On the other hand, the mesh applied to the background was coarser than that applied to the inclusion to improve the computational speed. To induce a lateral shear deformation, the bottom surface was fixed and a lateral displacement was applied to the top surface, as shown in Fig. 2. The amount of lateral shear deformation is specified by the lateral shear angle θ.

The FEA displacement field was then utilized in an ultrasound simulation program[38] to generate pre- and postdeformation rf echo signal data for elastographic processing. This program simulates the frequency domain response of ultrasound wave transmission through a scattering medium. The frequency response is then transformed back to the time domain to obtain ultrasound radio frequency frames. This simulation program achieves similar rf wave forms when compared to typical time domain simulation programs such as field II. In our simulation, a numerical phantom was constructed with scatterers modeled using 100 μm radius polystyrene beads, which were randomly distributed in the phantom at a number density of ten scatterers per cubic millimeter to ensure Rayleigh scattering.[27] The axial and lateral displacement fields from ANSYS, after appropriate interpolation to a regular Cartesian grid, were used to displace the scatterers and generate the deformed phantom to generate the postdeformation signals. A linear array transducer was modeled, which consisted of 0.1×10 mm^2 elements with a 0.1 mm center-to-center element separation. Each beam line was formed using 128 consecutive elements. The incident pulses were modeled to be Gaussian shaped with an 8-MHz center frequency and a 100% bandwidth. The simulations were performed assuming the sound speed in the phantom to be constant at 1540 m/s and attenuation to be negligible. The sampling frequency utilized was 52 MHz.

IV.B. Experiment

Two single-inclusion TM phantoms of size $10 \times 10 \times 10$ cm^3 manufactured in our laboratory were used to evaluate the proposed method. One of the phantoms contained a 1.4-cm diameter spherical inclusion fully bound to a uniform background, while the other phantom contained a 1.4-cm diameter spherical inclusion loosely bound to the background. Both inclusions were three times stiffer than the background. The inclusions correspond to simulated bound and unbound tumors surrounded by simulated breast glandular material background. The TM materials used in the phantom have been described previously[39,40] and consist of dispersions of microscopic safflower oil droplets in a (solid) aqueous gelatin matrix. In each phantom, the spherical inclusions are 10% oil by volume and the background is 50% oil by volume.

The basic method of production has been described previously,[40] but following is a brief summary. Two cubic acrylic boxes with inner dimensions $10 \times 10 \times 10$ cm^3 were produced. Saran Wrap® (Dow Chemical Co., Midland, MI) layers were epoxied over opposite ends of each box. Each box consisted of two identical parts, the box being cut by a plane parallel to the two parallel Saran Wrap® layers. The first step in producing each phantom involved placing a mold over the open end of a half box. This mold is a flat acrylic plate with an acrylic hemispherical projection facing the $5 \times 10 \times 10$ cm^3 volume. All inner surfaces, including the hemisphere, were coated with a thin layer of petrolatum so that the TM material would not adhere to them, and a flat constraining plate was placed over the Saran Wrap® surface. A hole in one acrylic side of the container allowed molten background TM material to be introduced. The (molten) background TM material was made using the method described previously[39] and the half box was filled with it. Gelation and formaldehyde cross linking of the gelatin occurred overnight. On the same day that the background material had been produced, a 14 mm diameter spherical inclusion was made with the 10% oil material. Thus, the sphere and $5 \times 10 \times 10$ cm^3 background section were ready for the final step the following day.

For the phantom to contain the unbound (loosely bound) spherical inclusion, the 14 mm diameter inclusion was coated manually with a thin layer of petrolatum—roughly 0.2 mm in thickness. The plate with a hemispherical projection was carefully removed from the $5 \times 10 \times 10$ cm^3 block of background material and the petrolatum-coated sphere was placed into the hemispherical depression in the congealed background TM material. Then the other half of the $10 \times 10 \times 10$ cm^3 container was epoxied in place and the remaining volume filled with molten background material. After congealing and cross linking were complete, the Saran Wrap® layers were removed and the cylindrical filling plug severed, allowing the $10 \times 10 \times 10$ cm^3 phantom to be removed from the acrylic container. The phantom was then submerged in oil in a covered container.

The production of the other phantom in which the spherical inclusion was to be bound to the background TM material proceeded in a different fashion. A small quantity (about 100 mL) of molten background TM material (50% oil) was produced and some of this material was drawn into a syringe. A drop of this "glue" was placed in the hemispherical depres-
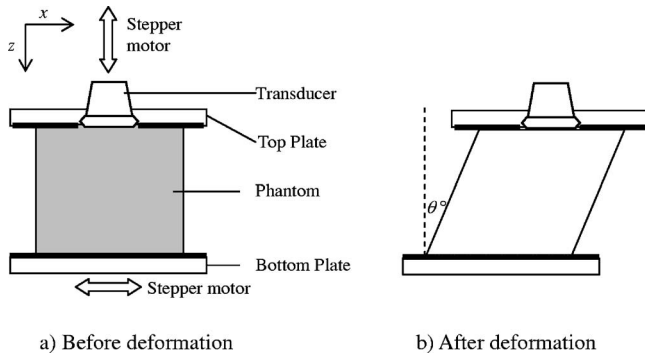
FIG. 5. A schematic diagram for the experimental setup for shear strain imaging by applying a lateral shear deformation.
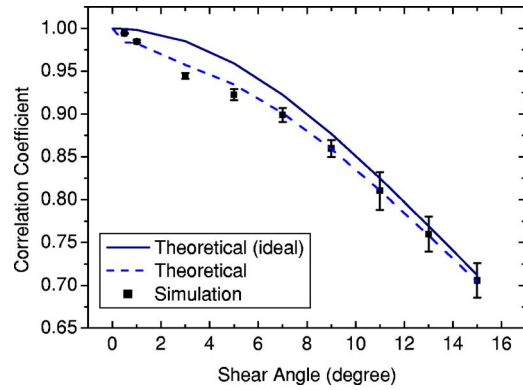

FIG. 6. Comparison between theoretical prediction and simulation results for the correlation coefficient of pre- and postdeformation rf segments as a function of applied shear deformation. The error bars were obtained from 12 independent realizations.

sion in the previously made $5 \times 10 \times 10$ cm³ section of background material and the 14 mm inclusion quickly was pressed into the hemispherical depression before any congealing of the glue had occurred. The glue congealed within a few seconds. Then the other half of the $10 \times 10 \times 10$ cm³ container was epoxied to the first half (containing the congealed TM background and spherical inclusion) and the remainder of the $10 \times 10 \times 10$ cm³ volume filled with molten background material. On the next day, the completed phantom was removed from its acrylic container (as described above) and submerged in safflower oil in a covered storage container.

The TM phantoms were scanned using a Siemens Antares real-time clinical scanner (Siemens Ultrasound, Mountain View, CA) equipped with a VFX 9-4 linear-array operating at 9 MHz. Digitized echo signals at a sampling rate of 40 MHz were acquired. To induce a lateral shear deformation, the phantom was placed on a plate attached to a stepper motor that introduces a specified lateral translation of the phantom and plate. The top surface of the phantom was fixed using a compression plate with a rectangular slot for the transducer face mounted on a linear stage driven by a second stepper motor that is translated in the axial direction. The surface of both plates was machined to be coarse to prevent any slipping between the plate and the phantom. The experimental setup is shown in Fig. 5. The phantoms were slightly compressed by the top plate to ensure contact and the predeformation rf data were obtained. The bottom plate was then laterally translated by a 2 mm increment corresponding to 1.3-deg shear angle and the postdeformation rf data acquired.

IV.C. Shear strain estimation

Axial and lateral displacements from the simulated and experimental phantoms were estimated using a two-dimensional multilevel motion tracking algorithm.[41] The first step of this algorithm involves an estimation of a coarse displacement estimate utilizing B mode or envelope signals. This coarse displacement estimate is then used to guide the final cross-correlation computations on rf data. In this study, we used a one-dimensional kernel, which is approximately 3 mm in the axial direction and one A line along the lateral direction, to compute the cross-correlation function and to

determine the displacement. For each step of this algorithm, the cross-correlation coefficient is used as the matching criteria. Components of the shear strain tensor as given in Eq. (25), including the axial shear (first term) and lateral shear strains (second term), are obtained from the displacement vectors. Partial derivatives are approximated using a least-squares strain estimator.[42]

IV.D. Results

Theoretical results demonstrating the variation in the correlation coefficient and the SNR_{sse} are verified and validated using simulated rf data obtained using a uniformly elastic phantom. Figure 6 shows a comparison between the theoretical prediction and simulation results for the correlation coefficient of pre- and postdeformation rf segments as a function of applied shear deformation. The correlation coefficient was obtained using a 3-mm rf data segment centered at a depth of 3 cm from the transducer. The error bars denote the standard deviation of the mean correlation coefficient estimates over 12 independent data sets, which were obtained using 12 independent realizations of the ultrasound simulation program with randomly distributed tissue scatterers. The theoretical prediction for the ideal case, obtained by computing Eqs. (16), (20), and (21), is plotted as a solid line. The theoretical prediction taking into consideration the effect of beam axis shift, obtained by computing Eqs. (16)–(20) and (23), is plotted as the dashed line. Here we assume that the shift is half the beam spacing $\Delta l = \Delta x / 2$. As illustrated in the figure, all curves follow a similar trend and the theoretical predictions agree with simulation results fairly well. Note that a better agreement between the theoretical prediction and simulation results is obtained when the Δl shift is considered, especially at small shear angles ($<7°$). This is because the beam axis shift effect is more pronounced for small lateral displacements, which is induced by a small amount of shear deformation. This can also be explained using Eq. (23), where the term $\Delta l / \tan \theta$ decreases with increasing shear angle.
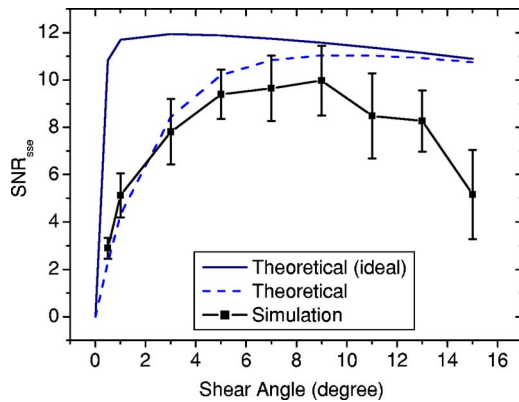
FIG. 7. Comparison between theoretical prediction and simulation results for the SNR_{sse} as a function of applied shear deformation. For simulation results, the SNR_{sse} was calculated using a rectangular ROI of 4×1 mm^2 at the center of shear strain images. The error bars were obtained from 12 independent realizations.

Figure 7 presents a comparison between theoretical predictions and simulation results for the SNR_{sse} as a function of the applied shear deformation. For simulation results, the SNR_{sse} was calculated using a rectangular ROI of 4×1 mm^2 at the center of shear strain images. The error bars were obtained from 12 independent realizations. Observe that the maximum SNR_{sse} is reached when the shear angle is around 3–5 deg for the simulation results. At smaller shear angles ($<7°$), as illustrated in the figure, the theoretical predictions (dashed line) show good agreement with simulation results when the beam axis shift effect is considered in our model. The theoretical curve for the ideal case, denoted by the solid line, however, overestimates the SNR_{sse} at small shear angles. This is due to the overestimation of the correlation coefficient at small shear angles when the beam axis shift is ignored, as shown in Fig. 6. At large shear angles ($>11°$), as shown in Fig. 7, simulation results for the SNR_{sse} are much lower than theoretical predictions. This is because

the theoretical model assumes that the displacement is accurately tracked while the simulation results contain large errors for displacement estimates due to signal decorrelation effects at large shear deformations.

Figure 8 presents the noise-free finite-element calculated shear strain images for both the bound inclusion (top) and the unbound inclusion (bottom) phantoms, induced with a lateral shear deformation with shear angle of 3°. Note that the presence of increased shear strains generated around the boundary between the inclusion and background for the unbound case. The difference in the shear strain patterns between bound and unbound cases is significant, when compared to the shear strain pattern difference shown in Fig. 1.

Figure 9 presents shear strain images calculated from US simulated rf data for the bound inclusion (top) and the unbound inclusion (bottom) phantoms. A lateral shear deformation with a shear angle of 3° was applied. Increased noise is observed in the image computed from lateral displacement. This is due to the lower resolution of displacement estimates in the lateral direction when compared to the axial direction. Although noisier, the shear strain images [(c) and (f)] exhibit similar patterns as shown in Figs. 8(c) and 8(f), and the difference between bound and unbound situations is clearly demonstrated.

Finally, Fig. 10 presents experimental shear strain images for both the bound and unbound spherical inclusion TM phantoms. A lateral shear deformation with shear angle 1.3° was applied. Observe that larger shear strains are generated around the boundary between the unbound inclusion and background when compared to the bound case. Note that the differences of shear strain patterns between bound and unbound cases are not so distinct compared to the simulation results shown in Fig. 9. This may occur because the experimental phantoms contain spherical inclusions instead of cylindrical inclusions used in our simulation models.
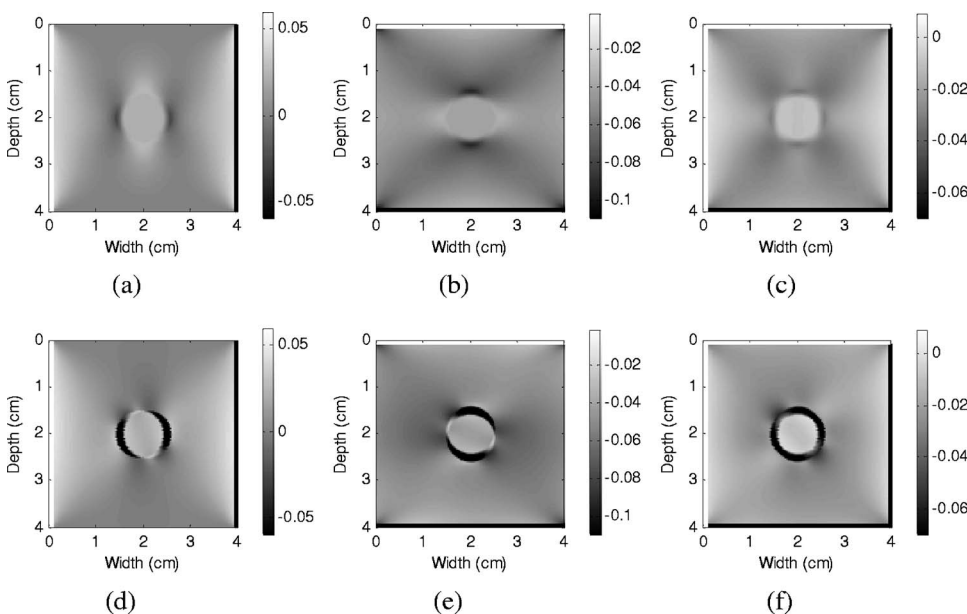

FIG. 8. Finite-element calculated images of [(a) and (d)] $\partial d_z / \partial x$, [(b) and (e)] $\partial d_x / \partial z$, and [(c) and (f)] shear strain $=0.5(\partial d_z / \partial x + \partial d_x / \partial z)$ for a fully bound inclusion (top) and an unbound inclusion (bottom) in a homogeneous background. A lateral shear deformation with $\theta=3°$ was applied.
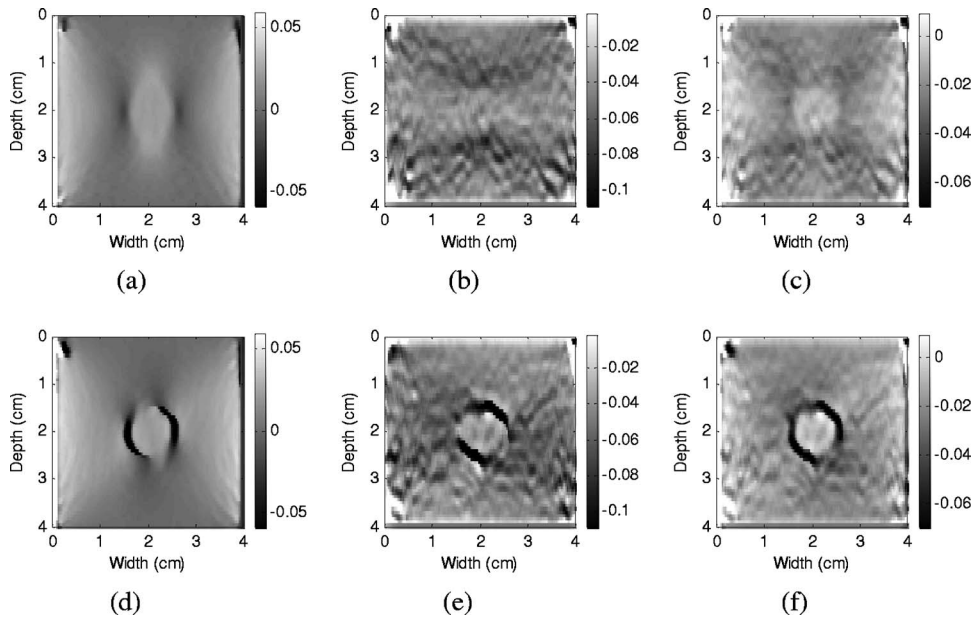
FIG. 9. Strain images generated from US simulated rf data of [(a) and (d)] $\partial d_z/\partial x$, [(b) and (e)] $\partial d_x/\partial z$, and [(c) and (f)] shear strain$=0.5(\partial d_z/\partial x +\partial d_x/\partial z)$ for a fully bound inclusion (top) and an unbound inclusion (bottom) in a homogeneous background. A lateral shear deformation with $\theta=3°$ was applied.

V. DISCUSSION

Shear strain elastograms provide useful additional information on the degrees of bonding and mobility between the tumor and surrounding tissues. Such information may help in the differentiation of benign from malignant tumors. Previously reported shear strain elastograms[12,43] were obtained from the axial and lateral displacement induced by an axial compression. In such cases, the shear strains not only depend on the bonding conditions, but are also related to their orientation with respect to the direction of compression. As shown in Fig. 1, although the magnitude of shear strains generated around an unbound inclusion is larger than that of the bound case, the shear strain patterns are still similar. This is due to the fact that the shear deformation at the boundary

of the inclusions is induced indirectly by the axial compression and the presence of the inclusion in both cases. Moreover, the extent of shear strains around the inclusion is fairly small and difficult to control. In this article, shear strain elastograms that are induced using a lateral shear deformation are presented. Simulation results demonstrated that the shear strain patterns for the bound and unbound inclusions are significantly different with lateral shear deformations. The amount of shear strains around the inclusion can also be directly controlled by the lateral shear angle applied to the phantom. Experimental results for both bound and unbound spherical inclusions using TM phantom are in agreement with the simulation results. These results indicate that the mobility of the malignant and benign tumors may be classi-
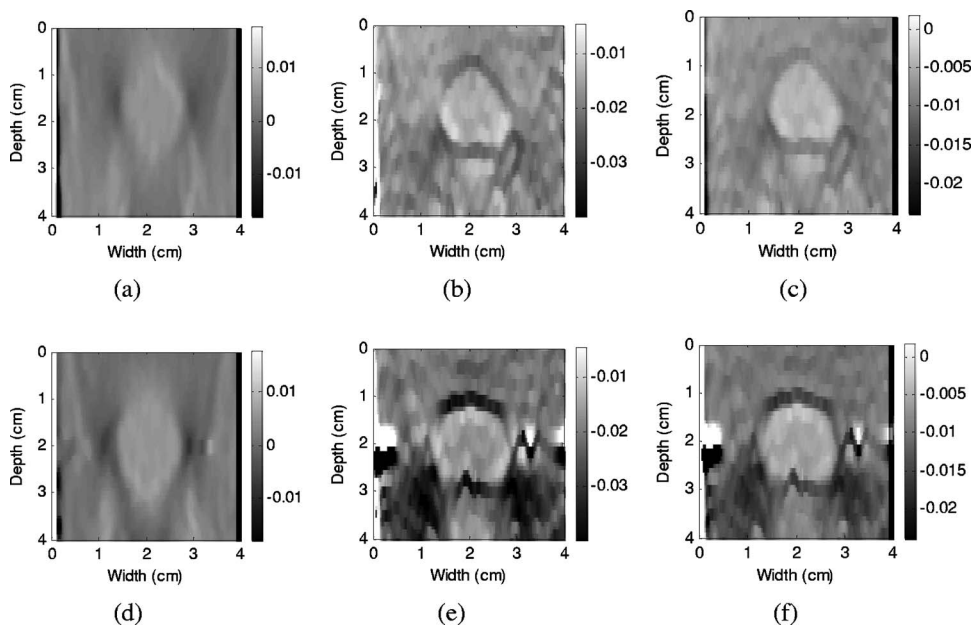

FIG. 10. Experimental images of [(a) and (d)] $\partial d_z/\partial x$, [(b) and (e)] $\partial d_x/\partial z$, and [(c) and (f)] shear strain $=0.5(\partial d_z/\partial x+\partial d_x/\partial z)$ for the bound inclusion phantom (top) and the unbound inclusion phantom (bottom). A lateral shear deformation with $\theta=1.3°$ was applied.

fied more clearly and directly through their shear strain patterns induced by a shear deformation instead of by axial compression.

To evaluate the quality of SSEs, a theoretical framework is established to study the correlation coefficient between the pre- and postdeformation rf data as a function of the applied shear angle. It is extended from our previous work[35,44] on the correlation analysis of rf echo signals obtained at different angular insonifications. The theoretical derivations are corroborated using US simulation results using a uniform phantom that verify and validate the theoretical expressions derived in the article. The decorrelation rate of the rf signal pairs before and after the shear deformation increase with applied shear angle as expected. This increased decorrelation rate is due to the cross-beam motion of scatterers following the applied shear deformation. This theoretical model also can be used to study the effect of the variation both the ultrasound system parameters such as the center frequency, bandwidth, etc. and the signal processing parameters such as the window length and overlap of the rf data segments on the correlation coefficient.

With the derived correlation coefficient, the lower bound on the standard deviation of the shear displacement estimates can be obtained through the ZZLB equations derived of the strain filter framework.[36] Thus, the upper bound on the SNR_{sse} of the SSE can be obtained in a similar way to that derived for normal strain tensor estimations. US simulation results using a uniform phantom are presented that verify the theoretical predictions of the SNR_{sse}. As shown in Fig. 7, the SNR_{sse} of simulation results increases to a maximum and starts to saturate around a shear angle of $3° - 5°$. A similar trend is also predicted by the theoretical results if the effect of the beam axis shift is taken into account in our model. For small shear deformations, the induced shear strain is low and leads to low SNR_{sse} values for the SSE. With an increase in the applied shear deformation, the SNR_{sse} improves with the increased shear strains. However, for very large lateral shear angles ($>11°$), shear decorrelation noise becomes significant leading to estimation errors in displacement estimates and the subsequent decrease in the SNR_{sse} at large shear deformations as shown in Fig. 7. Although the theoretical prediction overestimates the SNR_{sse} at very large shear angles, the model is still useful for choosing an optimal shear angle to obtain good shear strain images. Since the decorrelation rate depends on system parameters such as the center frequency and the window length, the optimal shear angle should be chosen depending on these parameter values. In addition, it is important to take into consideration the effect of the beam axis shift especially at small shear angles, as shown in Fig. 7.

VI. CONCLUSION

Shear strain elastograms induced using lateral shear deformation are investigated in this article. Ultrasound simulation results demonstrate that the shear strain patterns obtained by applying a shear deformation show significant differences between bound and unbound inclusion phantoms compared to shear strain images induced with axial compres-

sions. The amount of the shear deformation can also be easily controlled by varying the lateral shear angle. Shear strain imaging may be useful for clinical applications in differentiating malignant from benign tumors. A theoretical framework is also established to evaluate the variation in the correlation coefficient between pre- and postshear deformation rf signals and the SNR_{sse} of shear strain elastograms. Our results indicate that an optimal shear angle exists that would enable the acquisition of high quality shear strain elastograms that depends on both the ultrasound system and signal processing parameters.

[a] Author to whom correspondence should be addressed. Telephone: (608)-265-8797; Fax: (608)-262-2413. Electronic mail: minrao@wisc.edu

[1] W. A. D. Anderson, *Pathology*, 2nd ed. (Mosby, St. Louis, 1953).

[2] R. Muthupillai, D. J. Lomas, P. J. Rossman, J. F. Greenleaf, A. Manduca, and R. L. Ehman, "Magnetic-resonance elastography by direct visualization of propagating acoustic strain waves," Science **269**, 1854–1857 (1995).

[3] J. Ophir, I. Cespedes, H. Ponnekanti, Y. Yazdi, and X. Li, "Elastography—A quantitative method for imaging the elasticity of biological tissues," Ultrason. Imaging **13**, 111–134 (1991).

[4] I. Cespedes, J. Ophir, H. Ponnekanti, and N. Maklad, "Elastography—Elasticity imaging using ultrasound with application to muscle and breast *in vivo*," Ultrason. Imaging **15**, 73–88 (1993).

[5] M. O'Donnell, A. R. Skovoroda, B. M. Shapo, and S. Y. Emelianov, "Internal displacement and strain imaging using ultrasonic speckle tracking," IEEE Trans. Ultrason. Ferroelectr. Freq. Control **41**, 314–325 (1994).

[6] T. A. Krouskop, D. R. Dougherty, and F. S. Vinson, "A pulsed Doppler ultrasonic system for making noninvasive measurements of the mechanical properties of soft tissue," J. Rehabil. Res. Dev. **24**, 1–8 (1987).

[7] D. B. Plewes, I. Betty, S. N. Urchuk, and I. Soutar, "Visualizing tissue compliance with MR imaging," J. Magn. Reson. Imaging **5**, 733–738 (1995).

[8] K. J. Parker, S. R. Huang, R. A. Musulin, and R. M. Lerner, "Tissue response to mechanical vibrations for 'sonoelasticity imaging'," Ultrasound Med. Biol. **16**, 241–246 (1990).

[9] B. S. Garra, E. I. Cespedes, J. Ophir, S. R. Spratt, R. A. Zuurbier, C. M. Magnant, and M. F. Pennanen, "Elastography of breast lesions: Initial clinical results," Radiology **202**, 79–86 (1997).

[10] R. Souchon, O. Rouviere, A. Gelet, V. Detti, S. Srinivasan, J. Ophir, and J. Y. Chapelon, "Visualisation of HIFU lesions using elastography of the human prostate *in vivo*: Preliminary results," Ultrasound Med. Biol. **29**, 1007–1015 (2003).

[11] T. A. Krouskop, T. M. Wheeler, F. Kallel, B. S. Garra, and T. Hall, "Elastic moduli of breast and prostate tissues under compression," Ultrason. Imaging **20**, 260–274 (1998).

[12] E. E. Konofagou, T. Harrigan, and J. Ophir, "Shear strain estimation and lesion mobility assessment in elastography," Ultrasonics **38**, 400–404 (2000).

[13] C. Cole-Beuglet, R. Z. Soriano, A. B. Kurtz, and B. B. Goldberg, "Fibroadenoma of the breast: Sonomammography correlated with pathology in 122 patients," AJR Am. J. Roentgenol. **140**, 369–375 (1993).

[14] P. Skaane and K. Engedal, "Analysis of sonographic features in the differentiation of fibroadenoma and invasive ductal carcinoma," AJR Am. J. Roentgenol. **170**, 109–114 (1998).

[15] F. Viola and W. F. Walker, "Shear strain elastography," Proc.-IEEE Ultrason. Symp. **2**, 1907–1911 (2002).

[16] A. T. Kumar, J. Ophir, and T. A. Krouskop, "Noise performance and signal-to-noise ratio of shear strain elastograms," Ultrason. Imaging **27**, 145–165 (2005).

[17] W. F. Walker and G. E. Trahey, "A fundamental limit on delay estimation using partially correlated speckle signals," IEEE Trans. Ultrason. Ferro-

electr. Freq. Control **42**, 301–308 (1995).

[18]I. Cespedes, M. Insana, and J. Ophir, "Theoretical bounds on strain estimation in elastography," IEEE Trans. Ultrason. Ferroelectr. Freq. Control **42**, 969–972 (1995).

[19]M. Bilgen and M. F. Insana, "Error analysis in acoustic elastography. 1. Displacement estimation," J. Acoust. Soc. Am. **101**, 1139–1146 (1997).

[20]J. Meunier and M. Bertrand, "Ultrasonic texture motion analysis—Theory and simulation," IEEE Trans. Med. Imaging **14**, 293–300 (1995).

[21]M. Bilgen and M. F. Insana, "Deformation models and correlation analysis in elastography," J. Acoust. Soc. Am. **99**, 3212–3224 (1996).

[22]F. Kallel and J. Ophir, "Three-dimensional tissue motion and its effect on image noise in elastography," IEEE Trans. Ultrason. Ferroelectr. Freq. Control **44**, 1286–1296 (1997).

[23]E. Weinstein and A. Weiss, "Fundamental limitations in passive time delay estimation—Part II: Wide-band systems," IEEE Trans. Acoust., Speech, Signal Process. **32**, 1064–1078 (1984).

[24]A. H. Quazi, "An overview on the time-delay estimate in active and passive systems for target localization," IEEE Trans. Acoust., Speech, Signal Process. **29**, 527–533 (1981).

[25]C. H. Knapp and G. C. Carter, "The generalized correlation method for estimation of time delay," IEEE Trans. Acoust., Speech, Signal Process. **24**, 320–327 (1976).

[26]R. F. Wagner, M. F. Insana, and S. W. Smith, "Fundamental correlation lengths of coherent speckle in medical ultrasonic images," IEEE Trans. Ultrason. Ferroelectr. Freq. Control **35**, 34–44 (1988).

[27]R. F. Wagner, S. W. Smith, J. M. Sandrik, and H. Lopez, "Statistics of speckle in ultrasound -scans," IEEE Trans. Sonics Ultrason. **30**, 156–163 (1983).

[28]M. O'Donnell and S. D. Silverstein, "Optimum displacement for compound image generation in medical ultrasound," IEEE Trans. Ultrason. Ferroelectr. Freq. Control **35**, 470–476 (1988).

[29]S. W. Smith, R. F. Wagner, J. M. Sandrik, and H. Lopez, "Low contrast detectability and contrast detail analysis in medical ultrasound," IEEE Trans. Sonics Ultrason. **30**, 164–173 (1983).

[30]C. B. Burckhardt, "Speckle in ultrasound B-mode scans," IEEE Trans. Sonics Ultrason. **25**, 1–6 (1978).

[31]K. W. Ferrara and V. R. Algazi, "A statistical analysis of the received signal from blood during laminar flow," IEEE Trans. Ultrason. Ferro-

[32]B. H. Friemel, L. N. Bohs, K. R. Nightingale, and G. E. Trahey, "Speckle decorrelation due to two-dimensional flow gradients," IEEE Trans. Ultrason. Ferroelectr. Freq. Control **45**, 317–327 (1998).

[33]W. F. Walker and G. E. Trahey, "The application of k-space in medical ultrasound," IEEE Trans. Ultrason. Ferroelectr. Freq. Control **45**, 541–558 (1998).

[34]J. C. Bamber and J. V. Phelps, "The effective directivity characteristic of a pulsed ultrasound transducer and its measurement by semi-automatic means," Ultrasonics **15**, 169–174 (1977).

[35]Q. Chen, A. L. Gerig, U. Techavipoo, J. Zagzebski, and T. Varghese, "Correlation of RF signals during angular compounding," IEEE Trans. Ultrason. Ferroelectr. Freq. Control **52**, 961–970 (2005).

[36]T. Varghese and J. Ophir, "A theoretical framework for performance characterization of elastography: The strain filter," IEEE Trans. Ultrason. Ferroelectr. Freq. Control **44**, 164–172 (1997).

[37]E. E. Konofagou, T. Varghese, and J. Ophir, "Theoretical bounds on the estimation of transverse displacement, transverse strain and Poisson's ratio in elastography," Ultrason. Imaging **22**, 153–177 (2000).

[38]Y. Li and J. A. Zagzebski, "A frequency domain model for generating B-mode images with array transducers," IEEE Trans. Ultrason. Ferroelectr. Freq. Control **46**, 690–699 (1999).

[39]E. L. Madsen, M. A. Hobson, H. Shi, T. Varghese, and G. R. Frank, "Stability of heterogeneous elastography phantoms made from oil dispersions in aqueous gels," Ultrasound Med. Biol. **32**, 261–270 (2006).

[40]E. L. Madsen, M. A. Hobson, G. R. Frank, H. Shi, J. Jiang, T. Hall, T. Varghese, M. M. Doyley, and J. B. Weaver, "Anthropomorphic breast phantoms for testing elastography systems," Ultrasound Med. Biol. **32**, 857–874 (2006).

[41]H. Shi and T. Varghese, "Two-dimensional multi-level strain estimation for discontinuous tissue," Phys. Med. Biol. **52**, 389–401 (2007).

[42]F. Kallel and J. Ophir, "A least-squares strain estimator for elastography," Ultrason. Imaging **19**, 195–208 (1997).

[43]M. Rao, Q. Chen, H. Shi, T. Varghese, E. L. Madsen, J. Zagzebski, and T. A. Wilson, "Normal and shear strain estimation using beam steering on linear-array transducers," Ultrasound Med. Biol. **33**, 57–66 (2007).

[44]M. Rao and T. Varghese, "Correlation analysis of the beam angle dependence for elastography," J. Acoust. Soc. Am. **119**, 4093–4101 (2006).